

# Blind deconvolution for robust signal estimation and approximate source localization<sup>a)</sup>

Shima H. Abadi<sup>b)</sup>

*Department of Mechanical Engineering, University of Michigan, Ann Arbor, Michigan 48109*

Daniel Rouseff

*Applied Physics Laboratory, University of Washington, Seattle, Washington 98105*

David R. Dowling

*Department of Mechanical Engineering, University of Michigan, Ann Arbor, Michigan 48109*

(Received 13 August 2011; revised 16 January 2012; accepted 29 January 2012)

Synthetic time reversal (STR) is a technique for blind deconvolution in an unknown multipath environment that relies on generic features (rays or modes) of multipath sound propagation. This paper describes how ray-based STR signal estimates may be improved and how ray-based STR sound-channel impulse-response estimates may be exploited for approximate source localization in underwater environments. Findings are based on simulations and underwater experiments involving source-array ranges from 100 m to 1 km in 60-m-deep water and chirp signals with a bandwidth of 1.5–4.0 kHz. Signal estimation performance is quantified by the correlation coefficient between the source-broadcast and the STR-estimated signals for a variable number  $N$  of array elements,  $2 \leq N \leq 32$ , and a range of signal-to-noise ratio (SNR),  $-5 \text{ dB} \leq \text{SNR} \leq 30 \text{ dB}$ . At high SNR, STR-estimated signals are found to have cross-correlation coefficients of  $\sim 90\%$  with as few as four array elements, and similar performance may be achieved at a SNR of nearly 0 dB with 32 array elements. When the broadband STR-estimated impulse response is used for source localization via a simple ray-based backpropagation scheme, the results are less ambiguous than those obtained from conventional broadband matched field processing.

© 2012 Acoustical Society of America. [<http://dx.doi.org/10.1121/1.3688502>]

PACS number(s): 43.30.Cq, 43.30.Wi, 43.60.Jn [JIA]

Pages: 2599–2610

## I. INTRODUCTION

The acoustic signal from a remote source recorded by an underwater hydrophone array is commonly distorted by multipath propagation. Such recordings are the convolution of the source signal and the impulse response of environment at the time of signal transmission. Blind deconvolution is the name given to the task of determining the source signal and the impulse response from array-recorded sounds when the source signal and the environment's impulse response are both unknown. In general, blind deconvolution is ill posed as many possible signal and impulse-response pairs are mathematically possible for a single set of array recordings. Thus, additional information or assumptions are needed to reduce the solution space, and thereby produce unique and correct results.

Several blind deconvolution techniques for underwater acoustics have been developed in recent years. The virtual receiver algorithm uses a strategically located guide source, to remove many of the distorting effects of unknown multipath propagation (Siderius *et al.*, 1997). Blind deconvolution in multipath sound channels has also been studied under a

variety of statistical assumptions including, but not limited to, an adaptive super-exponential algorithm (Weber and Bohme, 2002), a least-squares criterion (Zeng *et al.*, 2009), a hypothesis regarding the form of the prior probability density function (PDF) of the input signal (Roan *et al.*, 2003), time-frequency signal processing (Martins *et al.*, 2002), and multiple convolutions (Smith, 2003). Related, blind source-separation techniques also seek to reconstruct source signals (Xinhua *et al.*, 2001).

Synthetic time reversal (STR) is a relatively simple technique that may be attractive for performing blind deconvolution in underwater sound channels in the bandwidth of the source signal to (1) determine the original source signal and the source-to-array impulse responses and (2) approximately localize the remote source. For the first of these two tasks, the additional information used in STR to uniquely estimate the source signal and the environment's impulse response is drawn from the generic characteristics of the acoustic modes (Sabra and Dowling 2004) or the acoustic rays (Sabra *et al.* 2010) that convey sound from the source to the array. Once mode- or ray-based propagation is assumed, no additional assumptions are needed about the form or statistics of the source signal or the environment's impulse response. Further, STR does not require parametric searches or optimization; its computational burden is only marginally greater than forward and inverse fast-Fourier transformation of the recorded signals. When the first-task effort is successful, the second task becomes possible when basic environmental characteristics

<sup>a)</sup>Portions of this work were presented at the 158th Meeting of the Acoustical Society of America, Baltimore, MD, May 2009, and the 159th Meeting of the Acoustical Society of America, San Antonio, TX, April 2010.

<sup>b)</sup>Author to whom correspondence should be addressed. Electronic mail: [shimah@umich.edu](mailto:shimah@umich.edu)

are known at the receiving array, and the range dependence of the underwater environment is mild.

Remote source localization is of continuing interest in a variety of sonar applications. In the last two or three decades, a variety of match-field processing (MFP) techniques have been shown to be successful when sufficient environmental information is available. MFP calculations were first conducted using normal modes (Bucker, 1976). The review article by Baggeroer *et al.* (1993) and the tenth chapter in Jensen *et al.* (1994) provide relevant background. The capability of the different MFP schemes to localize an unknown remote source under conditions of environmental mismatch is presented in Porter and Tolstoy (1994). A model-based matched filtering (MBMF) technique for source localization, involving cross correlations of measured and modeled signals, is described in Hermand and Roderick (1993). Source localization with horizontal arrays in shallow water is provided in Bogart and Yang (1994), and source localization based on eigenvalue decomposition is described in Benesty (1999). More recently, the maximum *a posteriori* estimator for MFP has been described in Harrison *et al.* (1998). Matched-field source localization using data-derived modes can be used to estimate both the wave numbers and bottom properties (Hursky *et al.*, 2001). At higher frequencies, the broadband match-field processing method presented in Hursky *et al.* (2004) is able to localize a remote sound source by cross-correlating measured and modeled impulse response functions and selecting the maximum cross-correlation peak. The coherent MFP method proposed in this paper is a variation of Hursky's algorithm with one difference: The actual impulse response was not measured; it was estimated by STR.

MFP and a variety of other techniques have also been used to estimate environmental parameters and the remote source location simultaneously. One such extension of MFP is focalization (Collins and Kuperman, 1991). Other relevant geoacoustic inversion schemes for using waterborne acoustic propagation data to determine the geoacoustic properties of the sea bottom are provided in Hermand and Gerstoft (1996), and Siderius and Hermand (1999). Notably, the MBMF technique can also be used for geoacoustic inversion (Hermand, 1999). Similarly, simultaneous estimation of the local sound speed profile and localization of a target on the ocean bottom in front of the host vehicle is possible using the adaptive bathymetric estimator (Cousins, 2005).

The purpose of this paper is to document how ray-based STR signal estimation depends on receiving array size and signal-to-noise ratio, how it can be improved through a coherent combination of results from individual rays, and how the STR-estimated impulse response can be used for source localization via matched-field processing or a simple ray-path backpropagation scheme. The results are based on simulations and experiments involving 1.5–4.0 kHz chirp signals propagating in a 60-m-deep sound channel at source array ranges of 100, 250, and 500 m. The accuracy of STR signal reconstruction is assessed via the cross-correlation coefficient with the original source signal. The accuracy of the various source localization results is assessed from distance differences between the estimated and actual source locations, and from the ambiguity surfaces' peak-to-side-lobe ratio.

The remainder of this paper is divided into five sections. The next section provides a short recap of the ray-based STR technique, including relevant formulas. The third section briefly describes the CAPEX09 experiment and presents beamforming results and sample signals. The fourth section provides results from simulations and the CAPEX09 experiments that illustrate how the ray-based-STR reconstructed signal,  $\hat{S}(t)$ , depends on the received signal-to-noise ratio, the number of array elements, and the source-array range. The fifth section describes how the STR-reconstructed impulse response can be used for simple ray-based backpropagation source localization, and documents how this simple technique compares to broadband Bartlett MFP in the same environment. The final section summarizes this research effort, and states the conclusions drawn from it.

## II. SYNTHETIC TIME REVERSAL

STR is a technique for simultaneously estimating the waveforms of the original source signal and the source-to-array transfer functions in an unknown underwater sound channel. In prior work STR was known as artificial time reversal. The mathematical formulation of propagating-mode-based STR is presented in Sabra and Dowling (2004) and its extension to acoustic rays is outlined in Sabra *et al.* (2010). Thus, for the present purposes, only final formulas are provided. A simple block-diagram description of STR and a generic blind deconvolution scheme is shown in Fig. 1. The inputs for STR are the measured waveforms  $P_j(t)$  from the  $N$  receiving-array elements located at  $\vec{r}_j$  ( $1 \leq j \leq N$ ), and the character of the acoustic propagation, modes or rays. The array-element weights  $W_j$  are chosen to isolate the propagation phase of a single mode or ray. The Fourier transform of the STR-estimated signal  $\hat{S}(\omega)$  and the STR-estimated impulse

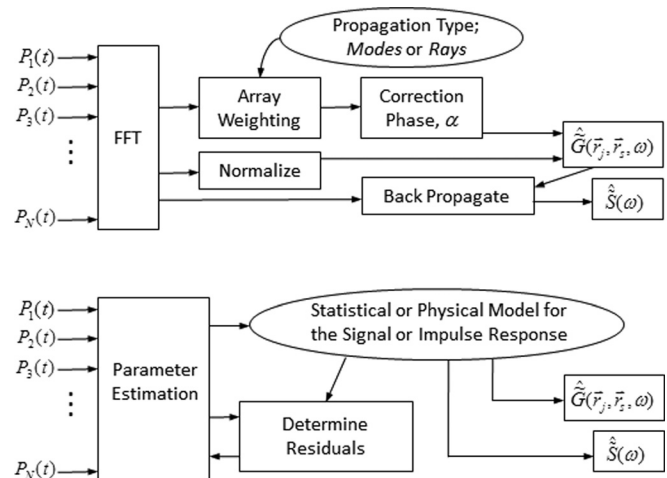


FIG. 1. Block diagrams for STR (above) and generic (below) blind deconvolution routines. In both cases the oval provides the additional information that allows the under-constrained blind deconvolution problem to be solved uniquely. In STR, the calculations proceed from left to right without feedback or iteration. In a generic blind deconvolution scheme, a statistical or physical model for the impulse response or the signal is used to reach unique results. Here the calculations may be more extensive as the model parameters typically must be optimized. In the lower block diagram, iterative optimization is depicted by the looping path of clockwise arrows between the oval and the two rectangles on the left.

response  $\hat{G}(\vec{r}_j, \vec{r}_s, \omega)$  between the source location  $\vec{r}_s$  and array-element locations  $\vec{r}_j$  are

$$\begin{aligned} \hat{S}(\omega) &= \sum_{j=1}^N \hat{G}^*(\vec{r}_j, \vec{r}_s, \omega) \tilde{P}_j(\omega) \\ &= \sum_{j=1}^N \left\{ \tilde{P}_j(\omega) e^{-i\alpha} / \sqrt{\sum_{k=1}^N |\tilde{P}_k(\omega)|^2} \right\}^* \tilde{P}_j(\omega), \end{aligned} \quad (1)$$

where

$$\alpha = \arg \left( \sum_{j=1}^N W_j \tilde{P}_j(\omega) \right). \quad (2)$$

Here,  $\tilde{P}_j(\omega)$  is the Fourier transform of  $P_j(t)$ ,  $\omega$  is the temporal frequency, an asterisk denotes a complex conjugate, a tilde denotes a frequency domain function, a caret denotes an estimated quantity, and  $\hat{G}(\vec{r}_j, \vec{r}_s, \omega)$  is the factor in curly braces in Eq. (1).

The weights  $W_j$  used to form the correction phase  $\alpha$  in Eqs. (1) and (2) are chosen empirically based on the receiving array's geometry and the character of the acoustic propagation. For situations involving a vertical line array with elements at depths  $z_j$  and modal propagation, the  $W_j$  can be selected to match the  $l$ th propagating mode:

$$W_j \propto \Psi_l(z_j), \quad (3a)$$

where  $\Psi_l(z)$  is the vertical profile of the  $l$ th propagating mode. For the same array geometry with propagation along acoustic rays, the  $W_j$  can be determined from plane-wave (or more sophisticated) beamforming:

$$W_j \propto \exp(-i\omega\tau(\theta_m, z_j)), \quad (3b)$$

where  $\tau$  is the time delay for the ray path that arrives at the  $j$ th receiver at nominal elevation angle  $\theta_m$  from the horizontal (see the upcoming Fig. 3), and the ray-path corresponding to  $\theta_m$  is called the reference ray. For simple plane-wave beamforming,  $\tau$  can be computed from

$$\tau(\theta, z_j) \cong (j-1)(d/\bar{c}) \sin \theta, \quad (4)$$

where  $\bar{c}$  is the depth-averaged speed of sound across the array and  $d$  is the distance between receivers. The possible values for  $\theta_m$  are determined from the maxima of the received beamformed energy:

$$B(\theta) = \int_{2\pi f_1}^{2\pi f_2} |b(\theta, \omega)|^2 d\omega, \quad (5)$$

where

$$b(\theta, \omega) = \sum_{j=1}^N \tilde{P}_j(\omega) \exp\{-i\omega\tau(\theta, z_j)\}, \quad (6)$$

the signal bandwidth is  $2\pi f_1 < \omega < 2\pi f_2$ , and  $|\theta| \leq \pi/2$ .

Inverse Fourier transformation of  $\hat{S}(\omega)$  and  $\hat{G}(\vec{r}_j, \vec{r}_s, \omega)$  produces the STR-estimated signal  $\hat{S}(t)$  and impulse response  $\hat{G}(\vec{r}_j, \vec{r}_s, t)$ . These time-domain results differ from the actual source signal and source-to-array impulse responses by a multiplicative amplitude scaling and an unknown time shift. Thus, direct estimates of the source-to-array range  $r$  are not possible based on *absolute* amplitude decay,  $|\tilde{P}_j/\hat{S}| \propto 1/\sqrt{r}$ , or the product of a nominal sound speed,  $c$ , and the *absolute* propagation time  $\Delta t$ ,  $r \approx c\Delta t$ , because  $|\hat{S}|$  and  $\Delta t$  remain unknown.

Yet, when STR is successful, the STR-determined waveforms, relative amplitudes, and *relative* timing between different acoustic ray (or modes) arrivals at the array are all correct. Thus, estimates of the source-to-array range are still possible using the travel-time *differences* between different acoustic modes or rays recovered from the STR-estimated impulse response. So, an unknown source that is not too distant from the array may be approximately localized by assuming a range-independent environment, computationally backpropagating impulses from the array launched with the STR-deduced time delays along the various ray paths, and then determining where in space the impulses most closely coincide as they propagate away from the array.

In this investigation, the source's signal and location with respect to the array are known, so the accuracy of the various estimates can be quantified. However, in applications of STR, this source information would not be known. Likewise, in a fully blind situation no environmental information would be known. However, source localization is not possible without some environmental information. Thus, to most closely mimic conditions in an actual application, the present investigation of localization performance assumes knowledge of only a minimal environmental parameter set at the array location: depths of the receiving phones, water column depth, speed of sound profile, and bottom type.

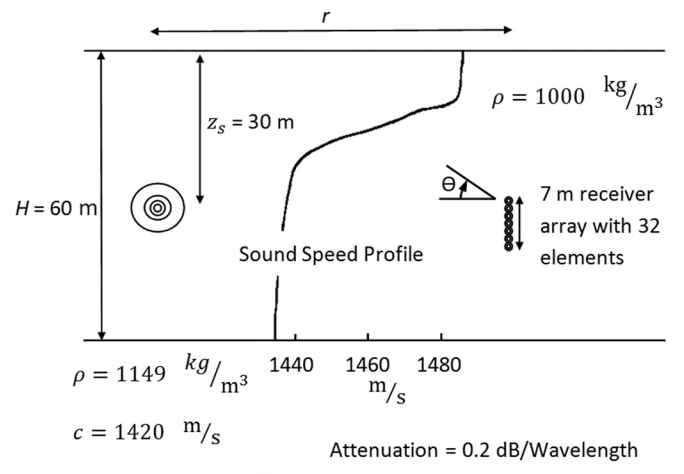


FIG. 2. Sound channel for the simulations and the experiments. Here the source depth is  $z_s = 30$  m and the primary source-array ranges for this study are  $r_s = 100, 250,$  and  $500$  m.

### III. CAPEX09 EXPERIMENT

The September 2009 Cooperative Array Performance Experiment (CAPEX09) was conducted in Lake Washington near Seattle (Rouseff *et al.* 2010). Two adjacent vertical receiving arrays of similar length were deployed from the stern of the two-point moored Research Vessel Robertson: A 32-element pressure-sensor array and an 8-element vector-sensor array. Each element of the vector-sensor array measured the acoustic pressure plus the three components of acoustic particle acceleration. Consequently, the two arrays made exactly the same number of acoustic measurements over similar vertical apertures. The source-to-array ranges varied between 10 m and 4 km in water nominally 60 m deep. A variety of signals were transmitted, but the present analysis is restricted to 50 ms duration frequency-modulated chirps sweeping linearly from 1.5 to 4 kHz with source depth 30 m. The analysis is further limited to data collected on the pressure-sensor array.

Figure 2 shows the measured sound speed profile in the water column together with other parameters from the

experiment. The contrast in sound speed between the warm surface water and the cool water below is more than 40 m/s resulting in sharp refraction of acoustic rays; ray traces (not shown) revealed that there was not a direct path uniformly across the entire array for ranges beyond  $\sim 400$  m. Figure 2 includes the 32-element pressure-sensor array shown to vertical scale. The top element was at nominal depth 30 m with uniform 22.4 cm spacing between the elements. As will be shown, the dense spacing of the array elements permits beamforming of the received chirp signals. The bottom properties were not measured during CAPEX09, but Lake Washington is known anecdotally to have a soft lakebed. Using numbers typical of sandy mud (see APL 1994), subsequent simulations assume the lakebed has sound speed 1420 m/s, density  $1149 \text{ kg/m}^3$ , and attenuation 0.2 dB/wavelength.

The recordings at range 10 m permit time gating of the direct signal to eliminate surface and bottom reflections. The resulting time-gated  $S(t)$  serves as the true signal against which the blind deconvolution results at much greater ranges

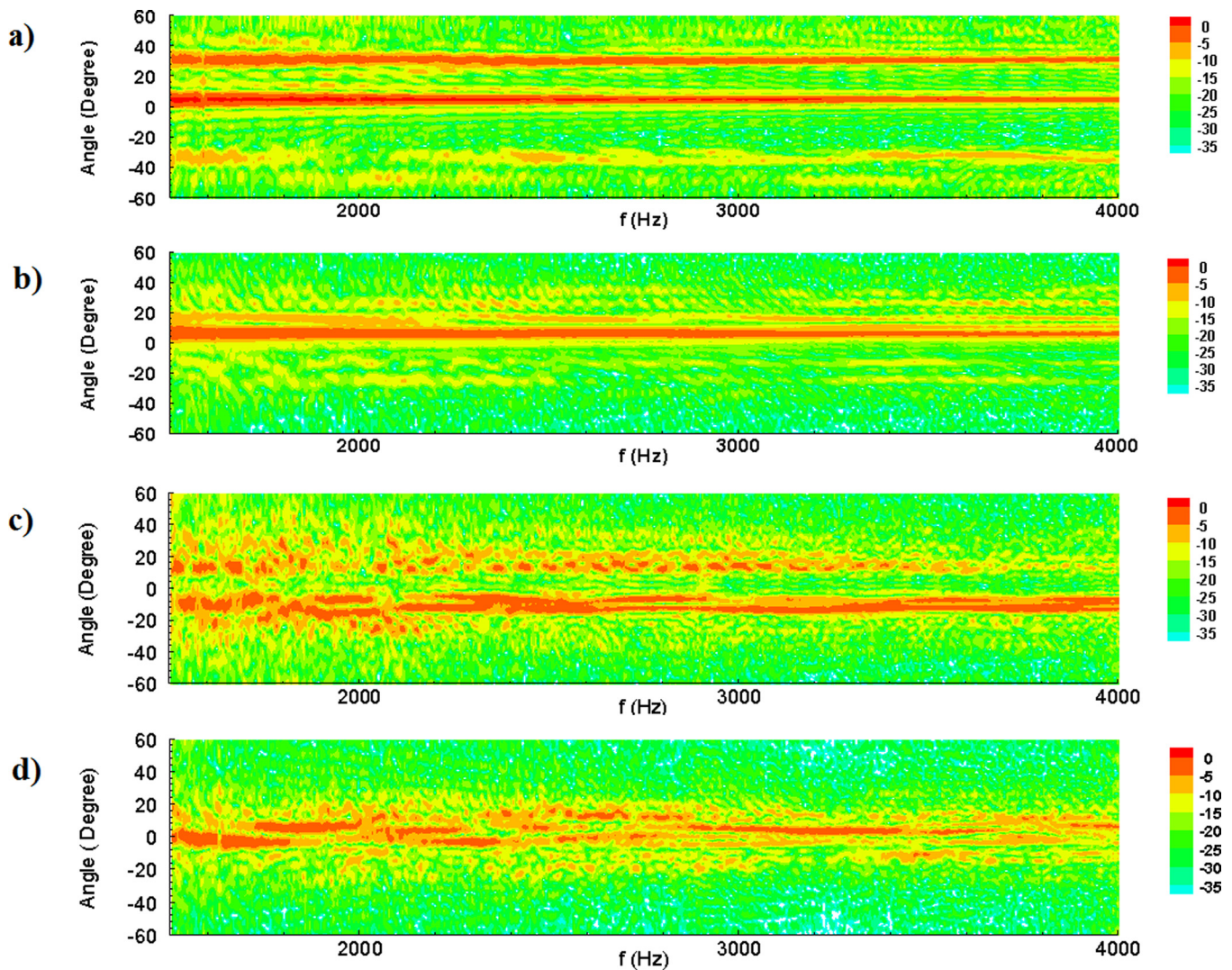


FIG. 3. (Color online) Magnitude of the beamformed output  $b(\theta, \omega)$  from the CAPEX09 receiving array at a source-array ranges of 100 m (a), 250 m (b), 500 m (c), and 1.0 km (d) as a function of frequency (Hz) and elevation angle (deg). Ray-based STR is successful when there is at least one distinct propagation path that persists at the same angle throughout the bandwidth of the signal. For these CAPEX09 measurements, STR works well at the shorter two ranges, has some success at 500 m, but fails at 1.0 km.

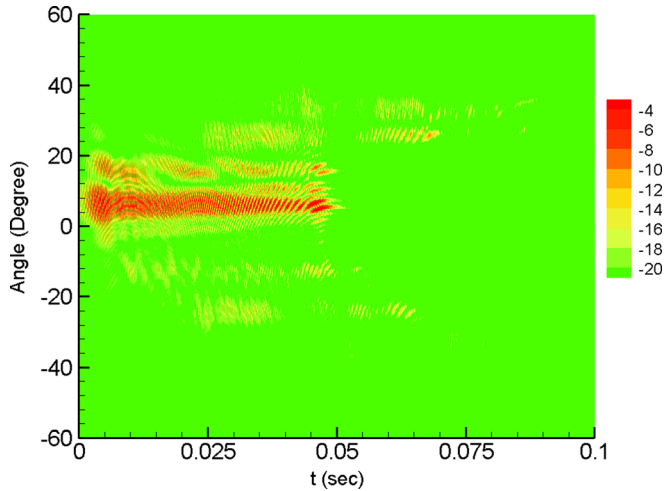


FIG. 4. (Color online) Absolute value of the time domain beamformed output  $b(\theta, t)$  from the CAPEX09 receiving array at a source-array range of 250 m as a function of time (s) and elevation angle (deg). The two main arrivals near  $7^\circ$  and  $16^\circ$  occur almost simultaneously. Weaker higher angle arrivals occur with delays of approximately 8, 20, and 40 ms.

are compared. Recordings at source-array ranges 100, 250, and 500 m are emphasized in the present study of STR performance.

Figure 3 illustrates propagation results via the beamformer output,  $|b(\theta)|$ , from the CAPEX09 experiment at source-array ranges of 100 m (a), 250 m (b), 500 m (c), and 1.0 km (d). The dynamic range shown in Fig. 3 covers 35 dB. At the 100 m source-array range, the direct path at  $5^\circ$

and surface-reflected path at  $30^\circ$  show up clearly throughout the signal bandwidth, whereas a weaker bottom reflection at  $-34^\circ$  is also apparent. At 250 m, the direct path with an arrival angle near  $7^\circ$  is the strongest, and several weaker paths exist within  $\pm 30^\circ$  or so of this direct path angle. At 500 m, there are two strong ray-path arrivals with angles that waver around  $-7^\circ$  and  $-12^\circ$  or so. Here again, several weaker paths at larger angles exist intermittently at the range. At 1.0 km, there are no ray-arrival angles that persist throughout the bandwidth of the signal. The recorded data at these four source-array ranges span the possible range of STR performance outcomes.

As a further illustration of the CAPEX09 data, Fig. 4 provides time-domain beamformed results [the absolute value of the inverse-Fourier transform of  $b(\theta, \omega)$  from Eq. (5)] at the 250 m range. Here the two primary arrivals can be seen to occur nearly simultaneously at arrival angles of  $\sim 7^\circ$  and  $\sim 16^\circ$ . In addition, there are several weaker larger-angle arrivals that are received with approximate time delays of 8, 20, and 40 ms.

Sample waveforms from this investigation are shown in Fig. 5 for the 250 m range when the direct path is selected as the reference ray. In Fig. 5, the first waveform [Fig. 5(a)] is the measured broadcast signal  $S(t)$ , the second waveform [Fig. 5(b)] is the signal recorded by the first (shallowest) element of the receiving array  $P_1(t)$ , the third waveform [Fig. 5(c)] is the output from a delay-and-sum beamformer with a receiving angle of  $6.7^\circ$ , the fourth waveform [Fig. 5(d)] is the STR-estimated signal  $\hat{S}(t)$  when all 32  $P_f(t)$  are utilized

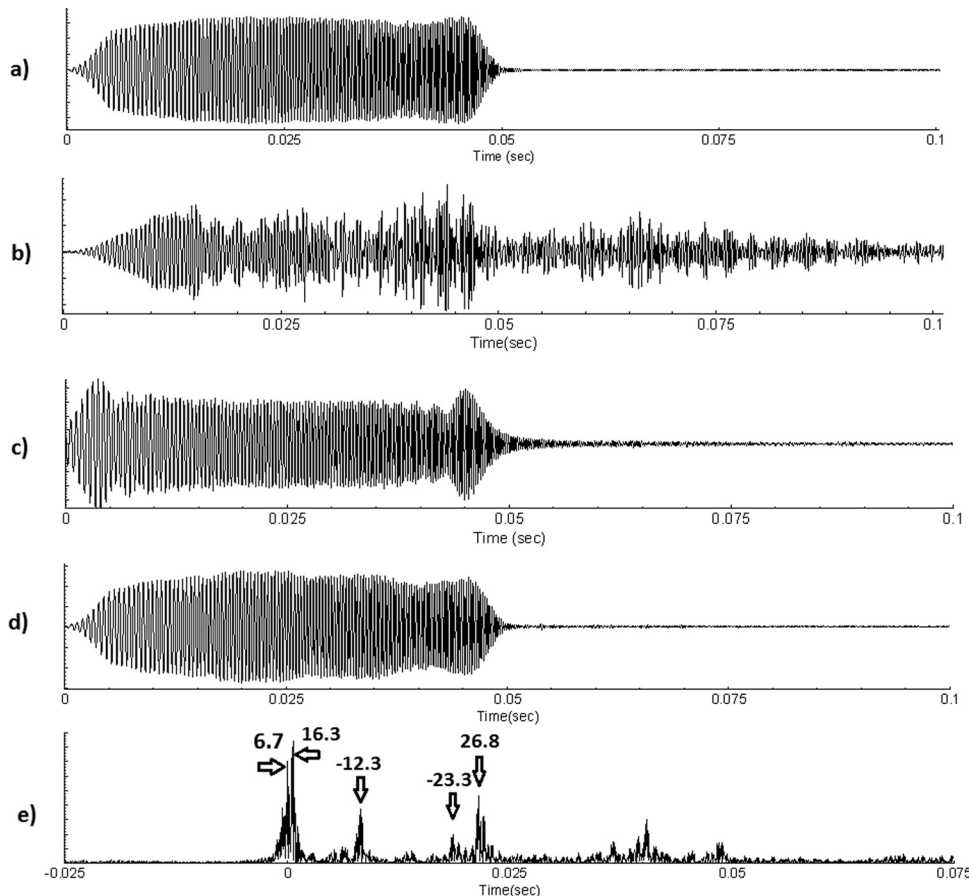


FIG. 5. Sample input and output signals for ray-based STR. (a) Measured broadcast signal, a nearly uniform amplitude sweep from 1.5 to 4.0 kHz with a duration of 50 ms. (b) Received signal at the shallowest array element at a range of 250 m. The cross-correlation coefficient of this signal with the broadcast signal is 57%. (c) Delay-and-sum beamformed output using the  $6.7^\circ$  ray-path shown in Fig. 3(b). The cross-correlation coefficient of this signal with the broadcast signal is 95%. (d) Ray-based STR estimated source signal using the  $6.7^\circ$  ray arrival shown in Fig. 3(b) as the reference ray. The cross-correlation coefficient of this signal with the broadcast signal is 99%. (e) Absolute value of the ray-based STR-estimated impulse response between the source and the shallowest array element using the  $6.7^\circ$  ray-path shown in Fig. 3(b) as the reference ray. The impulse response peak for this ray appears at  $t=0$ . The other impulse response peaks correspond to ray-arrival angles of  $16.3^\circ$ ,  $-12.3^\circ$ ,  $26.8^\circ$  and  $-23.3^\circ$ .

in the processing. Here, STR provides a noticeable improvement in the signal envelope shape over the single-receiver and delay-and-sum beamforming results because it coherently adds signal information from all propagation paths. Thus, ray-based STR can be considered an extension of delay-and-sum beamforming for blind deconvolution as it also provides an estimate of the source-to-array-element impulse responses that delay-and-sum beamforming does not provide.

The fifth waveform shown in Fig. 5(e), which has a 25 ms offset compared to the other waveforms, is the amplitude of the STR-estimated impulse response  $\hat{G}(\vec{r}_1, \vec{r}_s, t)$  between the source and the first array element at the 250 m range. The first important peak in this sample of  $\hat{G}(\vec{r}_1, \vec{r}_s, t)$  occurs at  $t=0$  and corresponds to the reference ray path ( $\theta_1 = 6.7^\circ$ ). The second, third, fourth, and fifth peaks correspond to ray paths with arrival angles of  $16.3^\circ$ ,  $-12.3^\circ$ ,  $-23.3^\circ$ , and  $26.8^\circ$  and signal-propagation times that are approximately 0.6, 8, 18, and 22 ms longer than that for the reference ray. If one of these other rays were chosen as the reference, the associated STR-estimated impulse response would place the peak for that ray at  $t=0$ . Although the absolute source-to-array travel time on any of these rays remains unknown, travel-time differences between ray paths are apparent.

#### IV. PARAMETRIC DEPENDENCIES OF STR SIGNAL RECONSTRUCTION

This section presents a variety of ray-based-STR signal-reconstruction performance results from the CAPEX09 experiment, and range-independent companion simulations using the ray propagation code BELLHOP (available from HLS Research, Inc.). The primary performance metric for signal reconstruction is the maximum cross-correlation coefficient (CCC),

$$\text{CCC} = \max_t \left( \frac{\int_{-\infty}^{+\infty} \hat{S}(\omega) \tilde{S}^*(\omega) e^{-i\omega t} d\omega}{\sqrt{\int_{-\infty}^{+\infty} |\hat{S}(\omega)|^2 d\omega} \sqrt{\int_{-\infty}^{+\infty} |\tilde{S}(\omega)|^2 d\omega}} \right), \quad (7)$$

between the broadcast signal  $S(t)$  and the STR-estimated signal  $\hat{S}(t)$ . For the data shown in Fig. 5, the peak CCCs of the original signal with the sample received signal, the delay-and-sum beamformed signal, and the STR-estimated signal are 57%, 95%, and 99%, respectively. In general, a CCC above 90% is needed for a blind deconvolution technique to be considered useful.

The parametric dependencies of STR's signal estimation performance are provided in Figs. 6–8. The first of these shows both simulation results (filled symbols) and experimental results (open symbols) for CCC from Eq. (7) as a function of the number of receivers ( $2 \leq N \leq 32$ ) for source array ranges of 100, 250, and 500 m. Here, for  $N < 32$ , contiguous array elements were used starting with the shallowest array element ( $j=1$ ); thus, the receiving array's aperture in Fig. 6 is directly proportional to  $N-1$  and increases downward from the shallowest element with increasing  $N$ . In

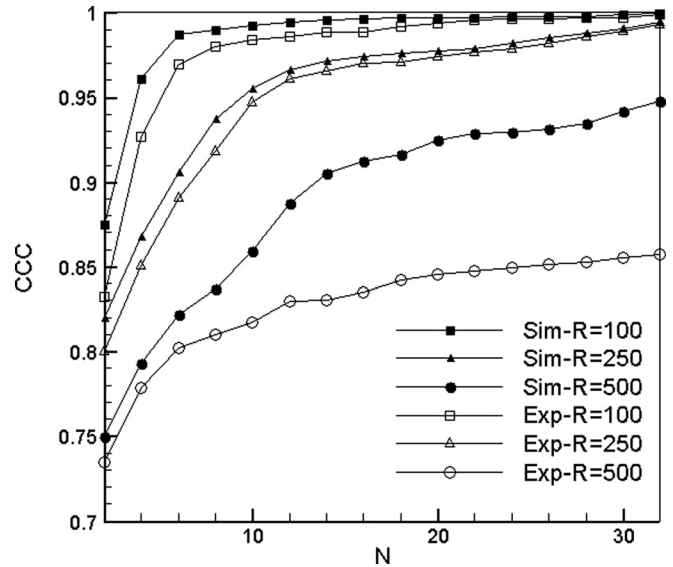


FIG. 6. Cross-correlation coefficient (CCC) from Eq. (7) for the simulations (filled symbols) and the CAPEX09 experiments (open symbols) for source-array ranges of 100, 250, and 500 m vs the number  $N$  of receiving array elements. Here CCC values increase with increasing  $N$ . STR's simulated and experimental performances match at the two shorter ranges, but differ by as much as 10% at the longer range.

all cases, STR's signal-estimation performance increases with increasing  $N$ , an array resolution effect. A longer array can better resolve ray-arrival directions, and thereby produce a better measurement of the requisite correction phase,  $\alpha$  in Eqs. (1) and (2). For the results shown in Fig. 6, reference ray-path arrival angles have been determined based on  $B(\theta)$  from all 32 elements and have not been altered for smaller  $N$ . Yet, it is potentially remarkable that greater than 90% signal CCC can be achieved at source-array ranges of 100 and 250 m with as few as 7 or 8 array elements. Further, at these ranges, the simulation and experimental CCC results are within 1% or 2% percent of each other and the residual small differences are most likely the mild detrimental effects of finite signal-to-noise ratio, weak random scattering in the experiments, or the limitations of plane-wave beamforming.

However, the simulated and experimental CCC results in Fig. 6 for the 500 m range differ by as much as 10% when  $N > 15$  or so, and this points to a limitation of ray-based STR. Its success depends on there being at least one ray-path arrival that persists with (nearly) constant  $\theta_m$  across the frequency range of the signal. An examination of the beamformed CAPEX09 signal shown in Fig. 3 supports this contention. At a source-array range of 100 m, there are two persistent ray paths. At 250 m [Fig. 3(b)], there is certainly one persistent ray-path arrival at  $\theta_m = 6.7^\circ$ . At 500 m [Fig. 3(c)], there is one or possibly two tenuously persistent arrivals that waver and intermittently disappear. At 1 km [Fig. 3(d)], there are no ray-path arrivals with sufficient persistence across the entire frequency band of the signal for successful ray-based STR.

The loss of persistent ray paths in the CAPEX09 data with increasing range may have both deterministic and random origins. First, the nominal resolution of the receiving array at the signal's band-center frequency is  $\sim 3^\circ$ . Thus, the receiving array may not fully distinguish the two wavering

ray paths with arrival angles near  $-10^\circ$  at the 500 m range. Second, based on eigenray calculations, the steep sound-speed gradient in the CAPEX09 environment causes different ray paths to reach the top and bottom of the array. Such differences in propagation characteristics were verified by separately beamforming the signal using the top and bottom halves of the array. As the current implementation of ray-based STR is built from plane-wave beamforming, its success is likely to be reduced in an environment where wavefront arrivals do not extend over the full spatial aperture of the receiving array. And finally, some random refraction and scattering is expected in the real underwater waveguide, but was not simulated. Such scattering increases in importance with increasing source-array range, and is likely to distort the signal wave fronts so they are no longer planar, the net result being a detrimental impact on ray-based STR performance that is only apparent in the experimental results.

A second limitation of STR arises from finite received signal-to-noise ratio (SNR). To quantify the impact of variable SNR on ray-based STR performance, noise samples  $n_j(t)$  measured at each receiver  $\sim 1/2$  s after reception of the CAPEX09 signal, and having the same duration as the received signals, were multiplied by a dimensionless coefficient  $\gamma > 0$  and added to the measured signal from each receiver. Thus, SNR, as defined by the following equation was varied artificially by increasing  $\gamma$ :

$$\text{SNR} = 10 \log \left\{ \frac{\int_{2\pi f_1}^{2\pi f_2} \sum_{j=1}^N \left[ |\tilde{P}_j(\omega)|^2 - |\tilde{n}_j(\omega)|^2 \right] d\omega}{(\gamma + 1) \int_{2\pi f_1}^{2\pi f_2} \sum_{j=1}^N |\tilde{n}_j(\omega)|^2 d\omega} \right\}. \quad (8)$$

Here  $\tilde{n}_j(\omega)$  is the Fourier transform  $n_j(t)$ . The measured noise spectra for some of the 32 elements include a single peak just above 2 kHz, but otherwise all were nearly flat through the signal bandwidth.

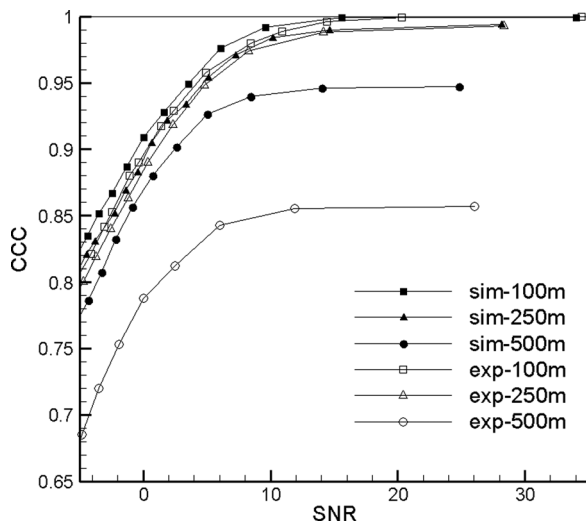


FIG. 7. Cross-correlation coefficient (CCC) from Eq. (7) for the simulations (filled symbols) and the CAPEX09 experiments (open symbols) for source-array ranges of 100, 250, and 500 m vs the SNR from Eq. (8). Here CCC values increase with increasing SNR. STR's simulated and experimental performance again matches at two shorter ranges, but differs by nearly 10% at the longer range.

The results of these variable SNR studies are shown in Fig. 7 where CCC is plotted vs SNR from Eq. (8) for the simulations and the experiments at source array ranges of 100, 250, and 500 m when all 32 receiving array elements are used. In all cases, CCC increases monotonically with increasing SNR. The simulation and experimental results at the shorter two ranges all fall within  $\pm 1\%$  of each other, and STR achieves a CCC of greater than 90% at a SNR of  $+2$  dB. The longer-range simulation and the experimental results fall below the others because the resolution requirements for achieving any fixed CCC value increase with increasing range, and because the received field in the experiment has only tenuously persistent ray-path arrivals.

In a variety of other underwater sound propagation scenarios, more than one ray-path arrival can typically be identified at the receiving array. Thus, the possibility exists that the final STR output may be improved in finite SNR situations by separately using each persistent ray-path arrival as the reference and then coherently combining the various STR results. This possibility was considered for the experimental data at the 100 m range where the direct and surface-reflected ray paths are well resolved, persistent, and of comparable strength. The STR CCC results using each path as the reference path are shown along with CCC results for a coherent combination of the path-specific results as a function of SNR on Fig. 8. Although the percentage differences are small, the coherent combination provides the highest CCC for all SNRs. Thus, improving STR results via a coherent combination of results from different reference rays is a promising possibility.

## V. STR AND SOURCE LOCALIZATION

STR can be used to estimate simultaneously the source signal and impulse response waveforms from a remote unknown source. Unfortunately, the unknown time shift in the reconstructed waveforms prevents elementary distance-equals-speed-times-time estimation of the source-array

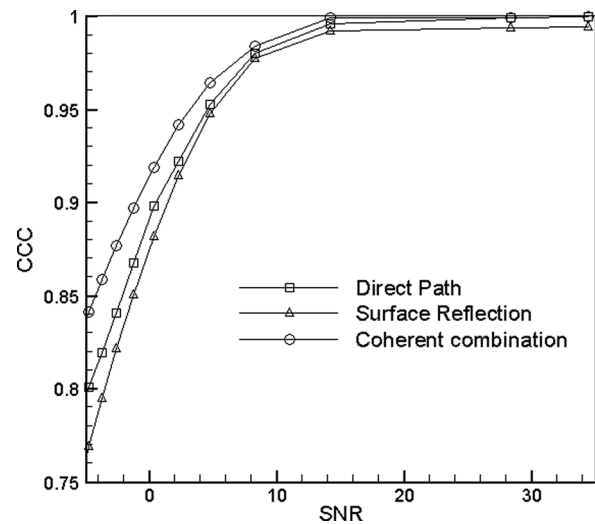


FIG. 8. Cross-correlation coefficient (CCC) from Eq. (7) vs SNR from Eq. (8) for the CAPEX09 experimental data at a source array range of 100 m. Here there are two persistent ray-path arrivals corresponding to direct and surface-reflected paths. A coherent combination of results from separate STR computations using each path as the reference is superior to that from either path alone.

range. However, the relative timing between peaks in the STR impulse response can be used to estimate the source range and depth when some environmental information is available. This possibility was explored using BELLHOP simulations and the CAPEX09 data set.

As a preliminary step, the correspondence between ray-path arrival angles and impulse response peaks must be determined. In the present study, this was done by inspecting  $B(\theta)$  to select possible ray-path arrival angles,  $\theta_m$  with  $1 \leq m \leq M$ , where  $B(\theta)$  showed a local maximum, and then completing  $M$  STR calculations to determine the impulse response peak corresponding to each  $\theta_m$ . When a valid  $\theta_m$  is used as the reference-path arrival angle, the impulse response peak associated with that path appears at the time origin when  $\hat{G}(\vec{r}_j, \vec{r}_s, t)$  is plotted vs  $t$ . For example, Fig. 5(e) displays  $|\hat{G}(\vec{r}_j, \vec{r}_s, t)|$  for the shallowest receiver at a source-array range of 250 m when an angle of  $6.7^\circ$  is used for the reference ray path. Here, the first peak of  $|\hat{G}(\vec{r}_j, \vec{r}_s, t)|$  occurs at  $t_1 = 0$  (the time origin) and this allows the identification  $\theta_1 = 6.7^\circ$ . The other impulse-response peaks occurring at  $t_m$  in Fig. 5(e) represent later arriving ray paths. If  $\theta_2 = 16.8^\circ$  had been chosen as the reference ray-path, then the second impulse response peak in Fig. 5(e) would have appeared at the time origin. The time-domain beamformed output is also able to link the arrival time and angle of each propagation path, as illustrated in Fig. 4 for the 250 m range. Once all possible ray-path arrival angles have been considered, the arrival angles  $\theta_m$  and STR-estimated relative time shifts  $t_m - t_1$  for the various paths connecting the source and the array are known. In a multipath environment, this angle and timing information is a signature of the source location, and this location may be estimated when there is enough environmental information for propagation calculations.

Three possible schemes for source localization are considered here: Simple ray-based backpropagation along identified rays, and conventional incoherent and coherent Bartlett matched field processing. For all three techniques, the environment is assumed to be range independent and the environmental information is limited to receiver depths, water column sound speed profile at the array, water depth at the array, and generic bottom type at the array. Thus, all three techniques are equally challenged by mismatch between the computational and actual environments. The formulation of the three techniques used in the present study is described in the next two paragraphs.

The ray-based backpropagation technique is based on acoustic time reversal (or phase conjugation in the frequency domain). First, the environmental information and the ray-arrival angles are used to compute  $M$  rays launched at angles  $\theta_m$  starting from the center of the array and extending out to the largest array-source range of interest, about 600 m in the current investigation. Next, the STR-determined impulse response is idealized as a series of perfect impulses that occur with the STR-determined arrival-time differences. This series of impulses is then time-reversed and each impulse is launched along its associated ray path from the array. As the various impulses, located at range-depth coordinates  $(r_m, z_m)$  propagate away from the array along their corresponding rays, the root-mean-square (rms) impulse

position,  $\zeta = \left[ (1/M) \sum_{m=1}^M \left( (r_m - R)^2 + (z_m - Z)^2 \right) \right]^{1/2}$ , based on Euclidian distances from the impulse centroid  $(R, Z) = (1/M) \sum_{m=1}^M (r_m, z_m)$ , is monitored. The centroid location with the minimum  $\zeta$  within the domain of interest provides an estimate of the source location. An example of such a ray-based backpropagation calculation is shown in Fig. 9, where the impulse positions are shown for three different times. In Fig. 9, the array is on the left at  $r = 0$  and the three rays emerge from the array-center depth of 33.5 m. In this case, a global minimum of  $\zeta$  occurs when the impulse centroid is located at (27 m, 100 m) when the source was actually located at (30 m, 100 m). Although such a simple scheme can be refined and enhanced, its current formulation is computationally efficient as it merely requires backpropagation calculations along a few ray paths once  $\theta_m$  and  $t_m - t_1$  are determined.

Conventional broadband MFP provides a more sophisticated means of source localization, but involves a significant increase in computational effort. Here both incoherent and coherent MFP schemes were considered. The incoherent calculations utilized six frequencies (1.5, 2.0, 2.5, 3.0, 3.5, and 4 kHz) within the signal bandwidth and the ambiguity surface  $A_i(r, z)$  was determined from an incoherent sum of single-frequency results,

$$A_i(r, z) = \frac{1}{6} \sum_{k=1}^6 \frac{\left| \sum_{j=1}^N \tilde{P}_j(\omega_k) G_c^*(\vec{r}_j, \vec{r}_s; \omega_k) \right|^2}{\left( \sum_{j=1}^N |\tilde{P}_j(\omega_k)|^2 \right) \left( \sum_{j=1}^N |G_c(\vec{r}_j, \vec{r}_s; \omega_k)|^2 \right)}, \quad (9)$$

where  $G_c(\vec{r}_j, \vec{r}_s; \omega_k)$  is the calculated complex acoustic pressure at location  $\vec{r}_j$  and frequency  $\omega_k$  from a harmonic point

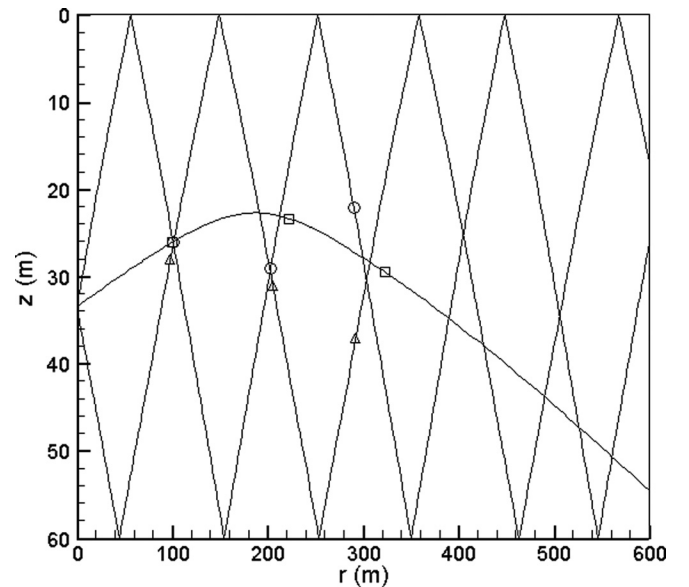


FIG. 9. Sample ray trace backpropagation calculation. The rays emerge from the center of receiving array at  $r = 0$  and  $z = 33.5$  m. Here symbols are shown at impulse locations at several different times when the rms impulse location,  $\zeta$ , achieves a local minimum. The actual source range and depth is 100 and 30 m, respectively.

source located at  $\vec{r}_s$ . The numerator of Eq. (9) amounts to a correlation between the measurements and the calculated impulse response across the array, whereas the denominator of Eq. (9) provides the appropriate normalization so that  $0 \leq A_i \leq 1$ .

The extension of Eq. (9) to broadband coherent Bartlett MFP involved field calculations throughout the signal bandwidth, and was formulated as a cross correlation between the STR-estimated impulse response and the computed impulse response,

$$A_c(r, z) = \max_t \left( \frac{\left| \int_{-\infty}^{+\infty} \hat{G}(\vec{r}_j, \vec{r}_s, \omega) G_c^*(\vec{r}_j, \vec{r}_s; \omega_k) e^{-i\omega t} d\omega \right|^2}{\left( \int_{-\infty}^{+\infty} |\hat{G}(\vec{r}_j, \vec{r}_s, \omega)|^2 d\omega \right) \left( \int_{-\infty}^{+\infty} |G_c(\vec{r}_j, \vec{r}_s; \omega_k)|^2 d\omega \right)} \right). \quad (10)$$

This formulation of coherent broadband MFP involving  $\hat{G}(\vec{r}_j, \vec{r}_s, \omega)$  is only possible when estimates of the source-to-array impulse responses are available.

The source localization results from the three techniques using the CAPEX09 data are provided in Fig. 10 for ray-based backpropagation, Fig. 11 for incoherent MFP from Eq. (9), and Fig. 12 for coherent MFP from Eq. (10). In Figs. 10–12, the panels (a)–(c) are for source-array ranges of 100, 250, and 500 m, respectively. The MFP results in Figs. 11 and 12 are presented in decibels,  $10 \log_{10}(A_i)$  and  $10 \log_{10}(A_c)$ , so that a perfect MFP localization result would produce a peak of 0 dB. In addition, the MFP results were computed with a range and depth resolutions of 5 m and 1 m, respectively.

Figure 10 shows the rms centroid distance  $\zeta$  from the ray-based backpropagation calculations as a function of source-array range. Although the results at each range display several local minima, the global minimum rms distance,  $\zeta_{\min}$ , in each case occurs unambiguously near the actual

source range. The alternative minima correspond to chance coalescence of the backpropagating impulses. For example, the three arrows shown on the top panel of Fig. 10 correspond to the marker locations shown in Fig. 9.

The MFP results in Figs. 11 and 12 are less decisive. Ambiguity surface values near or above that found close to the source location occur at multiple places within the spatial region considered. Mismatch between the actual and simulated environments is the likely reason for this indeterminacy. However, in all cases, an ambiguity-surface peak,  $(A_i)_p$  and  $(A_c)_p$ , can be found near the actual source location and these are marked by small black diamonds in Figs. 11 and 12. These marked peaks have decibel levels of  $-3$  to  $-10$ . The downward curving streak of high ambiguity surface values in parts (a) and (b) of Figs. 11 and 12 follows the direct ray path linking the source and the array. This streak is absent in part (c) of Figs. 11 and 12 because surface- and bottom-reflected ray paths primarily link the source and the array at the 500 m range.

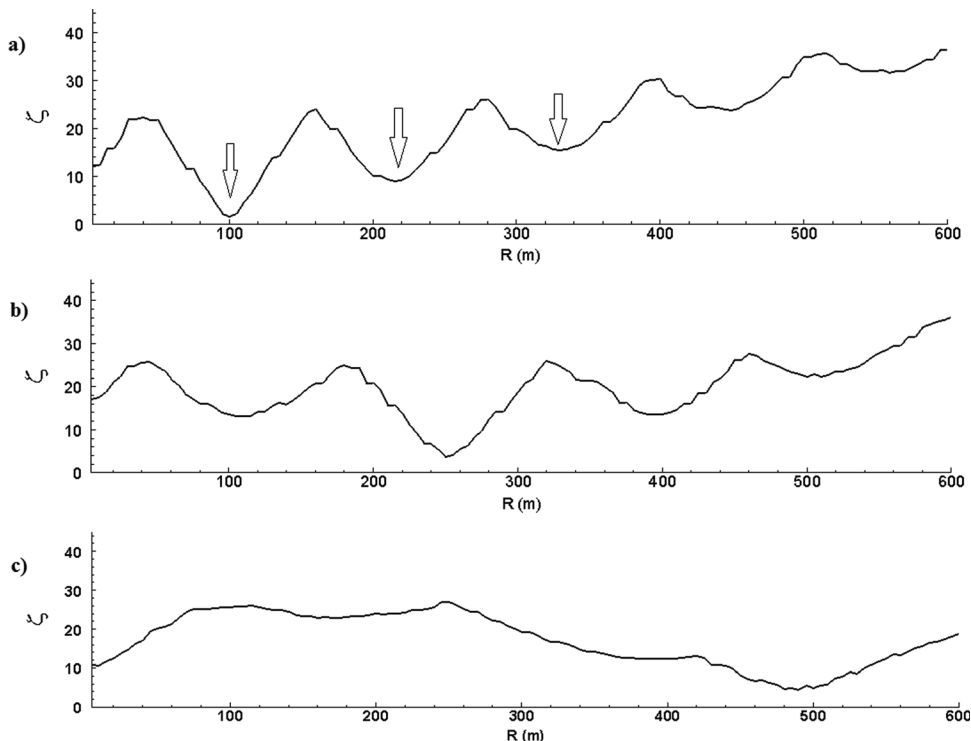


FIG. 10. Root-mean-square impulse location  $\zeta$  vs range for source-array ranges of 100 m (a), 250 m (b), and 500 m (c). Here the minimum  $\zeta$  unambiguously occurs near the actual source-array range. The arrows on the top panel lie at the ranges corresponding to the marker locations shown in Fig. 9.

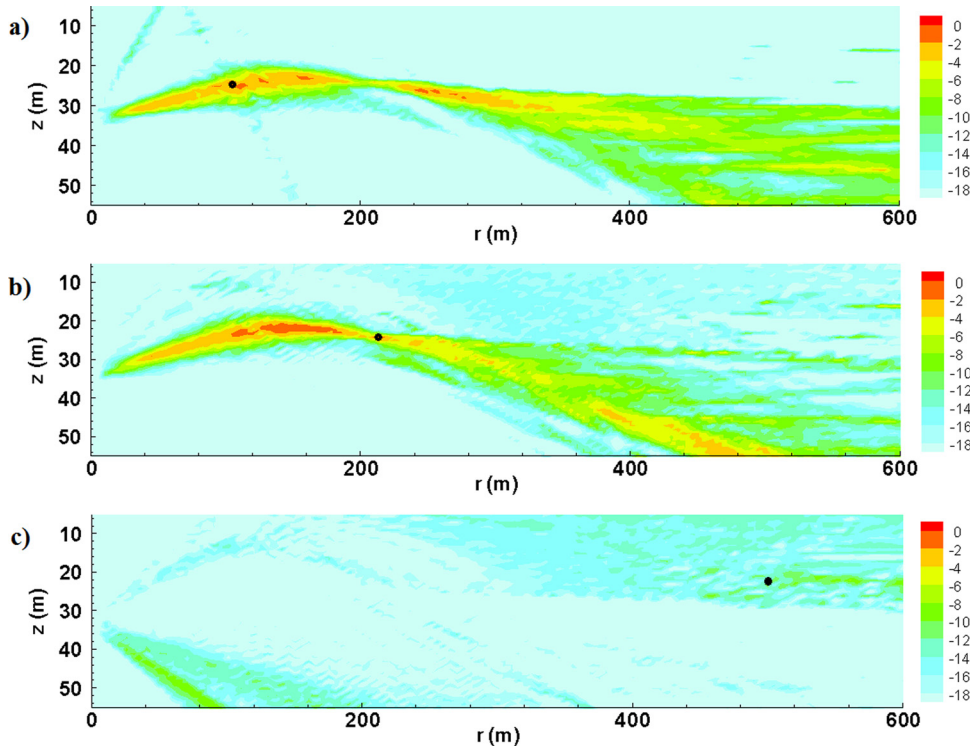


FIG. 11. (Color online) Ambiguity surface,  $A_i$ , for incoherent Bartlett matched field processing from Eq. (9) vs range and depth for source-array ranges of 100 m (a), 250 m (b), and 500 m (c). In this case, one or more peaks occur in  $A_i$  near the actual source range and depth. The small black diamond marks the ambiguity surface peak nearest to the source location.

Performance comparisons using  $\zeta_{\min}$  and the marked MFP peaks are provided in Table I, which lists extrema-to-side lobe ratios,  $\zeta_{\min}/\zeta_{\text{sl}}$ ,  $(A_i)_p/(A_i)_{\text{sl}}$ , and  $(A_c)_p/(A_c)_{\text{sl}}$ , range error, and depth error. The subscript “sl” in the prior listing and in Table I stands for *side lobe*. Overall, the three techniques provide comparable localization accuracy for the chosen ambiguity surface peaks. The tabulated source localization errors are acceptably small for the likely amount of mismatch between the actual and simulation

environments. However, there are at least two reasons to prefer the simple ray-based backpropagation approach. It is the least burdensome computationally, and, more importantly, it provides correct and unambiguous localization results when the MFP results do not. In particular, the peak-to-side-lobe ratio is near or below unity for all six MFP calculations, whereas the dynamic range between  $\zeta_{\min}$  and  $\zeta_{\text{sl}}$  is more than a factor of 2 for all three backpropagation calculations.

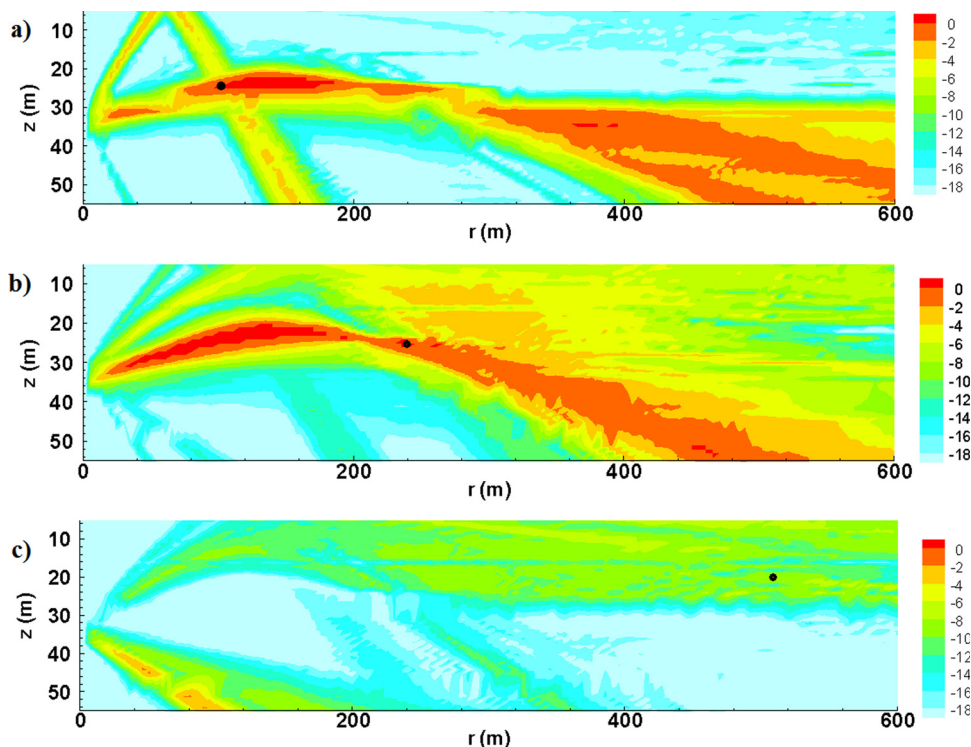


FIG. 12. (Color online) Same as Fig. 11 except the ambiguity surface,  $A_c$ , is shown for coherent Bartlett matched field processing from Eq. (10). Here again, peaks occur in  $A_c$  near the actual source range and depth. These results are based on the STR-estimated impulse response.

TABLE I. Localization performance comparisons.

|                                  | $R = 100$ | $R = 250$  | $R = 500$  |
|----------------------------------|-----------|------------|------------|
| Ray-based localization           |           |            |            |
| $\zeta_{\min}/\zeta_{\text{sl}}$ | 1.63/9.06 | 3.80/13.26 | 4.58/10.86 |
| Range error (m)                  | 0         | 0          | -10        |
| Depth error (m)                  | 3.3       | 1.5        | 6          |
| Incoherent MFP                   |           |            |            |
| $(A_r)_p/(A_r)_{\text{sl}}$      | 0.63/0.58 | 0.37/0.51  | 0.15/0.21  |
| Range error (m)                  | 5         | 10         | 0          |
| Depth error (m)                  | 6         | 5          | 7          |
| Coherent MFP                     |           |            |            |
| $(A_c)_p/(A_c)_{\text{sl}}$      | 0.60/0.62 | 0.53/0.68  | 0.25/0.41  |
| Range error (m)                  | 0         | 0          | 35         |
| Depth error (m)                  | 5         | 5          | 9          |

## VI. SUMMARY AND CONCLUSIONS

Synthetic time reversal (STR) is simple means for performing blind deconvolution in multipath environments that relies on generic characteristics of the acoustic rays (or modes) that connect the source and a receiving array to produce unique estimates of source-signal and impulse response waveforms. The current study focused on how array size, signal-to-noise ratio, and propagation characteristics influence the STR output; and on how STR impulse responses might be used to estimate the location of a remote unknown source. The results provided here are based on propagation simulations and underwater sound measurements involving a single source and a linear vertical receiving array at signal frequencies of several kilohertz and source-array ranges of 100 to 500 m in water that is 60 m deep.

The following conclusions can be drawn from this research effort. (1) Ray-based STR may be robust and effective with small vertical arrays that do not span the water column. STR with 32 array elements performs well ( $\text{CCC} \geq 90\%$ ) with measured additive noise at SNRs approaching 0 dB, and it performs similarly at high SNR with less than 10 array elements. In fact, as few as four or five array elements may be adequate in some circumstances. Even if the currently considered environment, signals, noise scaling, and array characteristics contribute favorably to the success of STR in this study, the present results—combined with those of prior STR studies in different environments with different signals—suggest that STR may be an effective means of blind deconvolution in a wide variety of multipath environments. (2) Ray-based STR is successful when at least one ray-path persists at a constant arrival angle throughout the bandwidth of the signal. It fails when there is no such ray path. Fortunately, the likelihood of STR failure because of this limitation can be anticipated by the presence or absence of persistent (angle-independent) ray-path arrivals in the beamformed array output as a function of frequency. Thus, in an application of ray-based STR, the user can independently determine whether or not STR results should be computed or trusted. (3) When two (or more) persistent ray arrivals are apparent in the beamformed signal, improvement to the STR output is possible when each persistent ray is used as the reference ray and these STR results are coher-

ently combined. (4) The STR impulse responses and simple ray-based backpropagation provide a relatively robust means for source localization when some environmental information is available at the receiving array. In the CAPEX09 environment, the source-localization capability of this simple technique was superior to broadband conventional MFP because it localized the source with acceptable accuracy without ambiguity. In addition, the computational burden for ray-based backpropagation is 2 or more orders of magnitude less than that for broadband MFP. Thus, it may provide a quick alternative to MFP, or it might be used to augment MFP results for a small increment in computational effort.

## ACKNOWLEDGMENT

This research effort was supported by the Office of Naval Research under Award No. N00014-05-1-0243.

- APL. (1994). “APL-UW high-frequency ocean environmental acoustic models handbook,” No. APL-UW TR 9407, Applied Physics Laboratory, University of Washington, Seattle, WA.
- Baggeroer, A. B., Kuperman, W. A., and Mikhalevsky, P. N. (1993). “An overview of matched field methods in ocean acoustics,” *IEEE J. Ocean. Eng.* **18**, 401–424.
- Benesty, J. (1999). “Adaptive eigenvalue decomposition algorithm for passive acoustic source localization,” *J. Acoust. Soc. Am.* **107**, 384–391.
- Bogart, C. W., and Yang, T. C. (1994). “Source localization with horizontal arrays in shallow water: Spatial sampling and effective aperture,” *J. Acoust. Soc. Am.* **96**, 1677–1686.
- Bucker, H. P. (1976). “Use of calculated sound fields and matched-field detection to locate sound sources in shallow water,” *J. Acoust. Soc. Am.* **59**, 368–373.
- Collins, M. D., and Kuperman, W. A. (1991). “Focalization: Environmental focusing and source localization,” *J. Acoust. Soc. Am.* **90**, 1410–1422.
- Cousins, D. B. (2005). “A model-based algorithm for environmentally adaptive bathymetry and sound velocity profile estimation,” Ph.D. dissertation, University of Rhode Island, Kingston, RI.
- Harrison, B. F., Vaccaro, R. J., and Tufts, D. W. (1998). “Robust matched-field localization in uncertain ocean environments,” *J. Acoust. Soc. Am.* **103**, 3721–3724.
- Hernand, J. P. (1999). “Broad-band geoacoustic inversion in shallow water from waveguide impulse response measurements on a single hydrophone: Theory and experimental results,” *IEEE J. Ocean. Eng.* **24**, 41–66.
- Hernand, J. P., and Gerstoft, P. (1996). “Inversion of broad-band multitone acoustic data from the YELLOW SHARK summer experiments,” *IEEE J. Ocean. Eng.* **21**, 324–346.
- Hernand, J. P., and Roderick, W. I. (1993). “Acoustic model-based matched filter processing for fading time-dispersive ocean channels: Theory and experiment,” *IEEE J. Ocean. Eng.* **18**, 447–465.
- Hursky, P., Hodgkiss, W. S., and Kuperman, W. A. (2001). “Matched field processing with data-derived modes,” *J. Acoust. Soc. Am.* **109**, 1355–1366.
- Hursky, P., Siderius, M., Porter, M. B., and McDonald, V. K. (2004). “High-frequency (8–16 kHz) model-based source localization,” *J. Acoust. Soc. Am.* **115**, 3021–3032.
- Jensen, F., Kuperman, W., Porter, M., and Schmidt, H. (1994). *Computational Ocean Acoustics* (American Institute of Physics, New York).
- Martins, N., Jesus, S., Gervaise, C., and Quinqu, A. (2002). “A time-frequency approach to blind deconvolution in multipath underwater channels,” in *International Conference on Acoustics, Speech, and Signal Processing*, Orlando, FL.
- Porter, M. B., and Tolstoy, A. (1994). “The matched-field processing benchmark problems,” *J. Comput. Acoust.* **2**, 161–185.
- Roan, M. J., Gramann, M. R., Erling, J. G., and Sibul, L. H. (2003). “Blind deconvolution applied to acoustical systems identification with supporting experimental results,” *J. Acoust. Soc. Am.* **114**, 1988–1996.
- Rouseff, D., Wang, Z., Zhou, S., and Zhou, L. (2010). “The 2009 Cooperative Array Performance Experiment (CAPEX09) comparing vector- and pressure-sensor arrays, in Proceedings of the European Conference on Underwater Acoustics (ECUA),” Istanbul, Turkey.

- Sabra, K. G., and Dowling, D. R. (2004). "Blind deconvolution in oceanic waveguides using artificial time reversal." *J. Acoust. Soc. Am.* **116**, 262–271.
- Sabra, K. G., Song, H. C., and Dowling, D. R. (2010). "Ray-based blind deconvolution in ocean sound channels," *J. Acoust. Soc. Am.* **127**, EL42–EL47.
- Siderius, M., and Hermand, J. P. (1999). "Yellow Shark Spring 1995: Inversion results from sparse broadband acoustic measurements over a highly range-dependent soft clay layer," *J. Acoust. Soc. Am.* **106**, 637–651.
- Siderius, M., Jackson, D. R., Rouseff, D., and Porter, R. (1997). "Multipath compensation in shallow water environments using a virtual receiver," *J. Acoust. Soc. Am.* **102**, 3439–3449.
- Smith, G. B. (2003). "Multipath compression by multiple convolutions," *J. Acoust. Soc. Am.* **113**, 2213.
- Weber, R., and Bohme, J. F. (2002). "Adaptive super-exponential methods for blind multichannel equalization," in *Sensor Array and Multichannel Signal Processing Workshop* (IEEE, New York), pp. 585–589.
- Xinhua, Z., Anqing, Z., Jianping, F., and Shaoqing, Y. (2001). "Study on blind separation of underwater acoustic signals," in *Proceedings ICSP2000* (IEEE, New York), pp. 1802–1805.
- Zeng, W.-J., Jiang, X., Li, X.-L., and Zhang, X.-D. (2009). "Deconvolution of sparse underwater acoustic multipath channel with a large time-delay spread," *J. Acoust. Soc. Am.* **127**, 909–919.